Development of a Dual-PIV system for high-speed flow applications

Anne-Marie Schreyer, Jean Lasserre, Pierre Dupont

Anne-Marie Schreyer, Jean Lasserre, Pierre Dupont. Development of a Dual-PIV system for high-speed flow applications. Experiments in Fluids, 2015, 56 (10), pp.187. 10.1007/s00348-015-2053-0 . hal-03763442

Experiments in Fluids manuscript No.
(will be inserted by the editor)

Development of a Dual-PIV system for high-speed flow applications

Anne-Marie Schreyer · Jean J. Lasserre · Pierre Dupont

Received: date / Accepted: date

Abstract A new Dual-Particle Image Velocimetry (Dual-PIV) system for application in supersonic flows was developed. The system was designed for shock-wave/turbulent boundary layer interactions with separation. This type of flow places demanding requirements on the system, from the large range of characteristic frequencies $O(100\,\mathrm{Hz}\ -100\,\mathrm{kHz})$ to spatial and temporal resolutions necessary for the measurement of turbulent quantities [1–3]. While classic PIV systems using high resolution CCD sensors allow high spatial resolution, these systems cannot provide the required temporal resolution. Existing high-speed PIV systems provide temporal and CMOS sensor resolutions, and even laser pulse energies, that are not adapted to our needs. The only obvious solution allowing sufficiently high spatial resolution, access to high frequencies, and a high laser pulse energy is a multi-frame system: a Dual-PIV system, consisting of two synchronized PIV systems observing the same field of view, will give access to temporal characteristics of the flow. The key technology of our system is frequency-based image separation: two lasers of different wave lengths illuminate the field of view. The cross-pollution with laser light from the respective other branches was quantified during system validation. The overall system noise was quantified and the prevailing error of only 2% reflects the good spatial and temporal alignment. The quality of the measurement system is demonstrated with some results on a subsonic jet flow including the spatio-temporal inter-correlation functions between the systems. First measurements in a turbulent flat-plate boundary layer at Mach 2 show the same satisfactory data quality and are also presented and discussed.

Keywords Dual–PIV · Supersonic flow · Turbulence

1 Introduction

The objective of the present study was the development and validation of a new Dual-PIV system for accurate measurements in turbulent high-speed flows, especially highly disturbed flow fields like shock wave/turbulent boundary layer interactions (SWTBLI). The flow field that we intend to investigate is a reflected plane shock interaction at Mach 2 with a large range of characteristic frequencies between $O(100\,\mathrm{Hz})$ for the shock motion and breathing pulsations of the separation bubble, $O(1-10\,\mathrm{kHz})$ for the large coherent scales developed in the interaction region, $O(10-50\,\mathrm{kHz})$ for large-scale coherent structures in the incoming boundary layer, and $O(100\,\mathrm{kHz})$ for the smaller turbulent scales [2]. See Figure 1 for a schematic drawing of the flow field.

To be able to accurately resolve the turbulent quantities, we require a spatial resolution of around 85 pixels per displacement thickness δ^* and a time delay between the two systems of around $O(\delta\tau) = 1\,\mu\mathrm{s}$. While classical Particle Image Velocimetry (PIV) using high resolution CCD sensors gives reliable spatially resolved data for both the mean and turbulent quantities, temporally

Anne-Marie Schreyer
Aix-Marseille Université, CNRS, IUSTI UMR 7343, 13013 Marseille, France,
Centre National d'Etudes Spatiales CNES, DLA, 75612 Paris Cedex, France
Current address: Institute of Fluid Mechanics, Technische Universität Braunschweig, 38108 Braunschweig, Germany
E-mail: anne-marie.schreyer@univ-amu.fr

Pierre Dupont
Aix-Marseille Université, CNRS, IUSTI UMR 7343, 13013 Marseille, France

Jean J. Lasserre
DantecDynamics, 2740 Skovlunde, Denmark

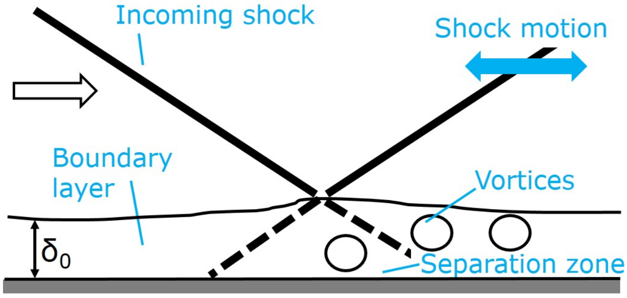

Fig. 1 Schematic drawing of the main flow features of a reflected shock interaction.

resolved systems are not available for the appropriate time scales in turbulent supersonic flows. Also high-speed or "time-resolved" PIV systems based on CMOS sensor solutions do not provide the necessary temporal resolution, sensor resolution, and laser pulse energies. Therefore, the only obvious solution allowing sufficiently high spatial resolution, access to small temporal scales (characteristic time scales of turbulence), and a high laser pulse energy is a multi-frame system, more specifically a Dual-PIV system. In principle, Dual-PIV systems consist of two independent, yet synchronized, PIV systems observing the same field of view. They allow the determination of certain temporal information also in high-speed flow, and give insight into the temporal development of the flow. Some Dual-PIV system setups were realized in other research groups, which, apart from laser power and spatial resolution, mainly differ in the approach used to separate the images from each other in CCD-based camera systems. Fleury et al. [4] describe a coupled system with two pulsed double-cavity Nd:YAG lasers operating at 532 nm and 50 mJ/pulse and two double frame CCD cameras, where a fast optical shutter is used with the first camera. The second laser is then triggered when this shutter is closed, allowing a minimal temporal delay of $\delta\tau = 20\,\mu$s between the two systems, which is not sufficient for our intended application. A more common technique, also allowing arbitrarily small time delays, is polarization-based image separation. The two laser beams are cross-polarized and the cameras are equipped with two different polarizers that either allow the passage of vertically or horizontally polarized light. Such systems are or have been in use for different applications, see Bridges & Wernet [5], Bridges [6], Guibert & Lemoyne [7] and Souverein et al. [8] and are also in use in dual-plane stereoscopic PIV setups (Ganapathisubramani et al. [9], Hu et al. [10], Kähler & Kompenhans [11], Kähler [12]). Polarization-based image separation is not always sufficiently effective, though. Also, polarization-based systems require spherical seeding particles to achieve good data accuracy and therefore droplets should be used [13]. We chose oil droplets from incense smoke as seeding material in our current application to be able to directly compare the new system with previous classical PIV systems. However, we were still interested in the development of a more versatile PIV system that could also be used with solid metal oxide seeding particles and in exothermic reacting flows. For the same reason, Mullin & Dahm [13] developed a frequency-based image separation system for their Dual Plane Stereo PIV setup. The two planes of interest were illuminated by laser light sheets with wave lengths of 532 nm and 635 nm, respectively, that were generated by dual head Nd:YAG lasers (532 nm) and two pulsed dye lasers (635 nm), which were again pulsed by two Nd:YAG laser tubes. Color filters on the lenses of the PIV cameras were applied to separate the images from each other. With this laser system, pulse energies of 40 mJ were obtained.

To summarize, in order to enable measurements of high quality in complex supersonic flow fields, like the reflected shock interaction we intend to investigate, the new system has to fulfill a number of major requirements: 1) Accurate resolution of the turbulent quantities – to achieve this, a spatial resolution of around 85 pixels per displacement thickness δ^* is required. 2) Capability to provide a field of view sufficiently large to show the interaction region and the incoming boundary layer. 3) The temporal delay between the systems has to be sufficiently small ($O(1\,\mu s)$) and adjustable to obtain temporal information in a high-speed flows, and 4) a low overall system-noise level, that is equal for both of the PIV systems. Furthermore, we required that both liquid seeding and solid seeding particles can be applied with the system.

2 Experimental setup and measurement principle of the Dual-PIV system

For the system developed at IUSTI in collaboration with DantecDynamics, we required largepulse energies to obtain sufficient illumination with the small seeding particles necessary in high-speed flow. Also, in order to obtain PIV data of high quality, we required two lasers with more similar characteristics and thus the same signal to noise ratio for both systems. Therefore, a dual head Nd:YAG laser operating at a wave length of 532 nm and a pulse energy of 200 mJ/pulse was used along with a specifically modified Nd:YLF laser, operating at an equally large pulse energy, but at the only slightly different wave length of 527 nm. This small difference in wavelength allows to generate light-sheets with similar properties for both PIV systems.

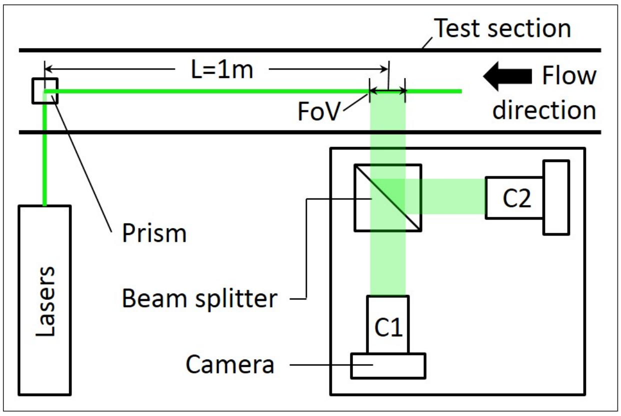

Fig. 2 Schematic of the Dual-PIV system at IUSTI

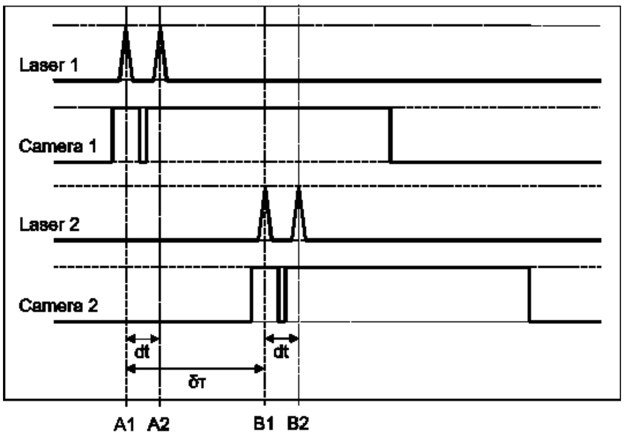

Fig. 3 Timing diagram of the DualPIV system.

For example, both systems are using lighsheets of similar thickness.

A schematic drawing of the experimental setup of the Dual-PIV system is shown in Figure 2. The two lasers are mounted on top of each other, the laser beams are carefully led along the same optical path by means of a beam combiner system, and a system of lenses with a confocal length of 5 mm and a divergence angle of 15° is applied to create the light sheets of 1 mm thickness. The light sheets illuminate the same field of view (FoV).

Essential for the functioning of the Dual-PIV measurement technique is the image separation system, for which optical color filters, one low-pass (frequency $f \leq 527\,\mathrm{nm}$) and one narrow band-pass filter ($f = 532\,\mathrm{nm}$, bandwidth of 3 nm), installed in front of the camera lenses, are applied in the current setup. The color filters are necessary to separate the images: the second camera frame does not shut immediately, but with a technically inevitable time–lag. Without the filters, for small temporal delays between the PIV systems, the second image frame would thus additionally capture the laser light corresponding to the second system (see Figure 3). Furthermore, the filters allow simultaneous acquisitions ($\delta\tau = 0$), which allows to estimate the signal to noise ratio of the system (see section 3).

Two high-resolution and high-sensitivity 4008×2672 pixels dual frame 11M pixel cameras with a minimum inter-frame delay of 200 ns and equipped with Zeiss 100 mm $f2$ objectives are used. The use of large sensor ($24 \times 36\,\mathrm{mm}$, 11 MPx) with high sensitivity CCD (Hisense 630 (PCO 4000)) cameras, combines large pixel size and high electronic sensitivity. The effect of peak-locking has been taken into account, and a spatial resolution of 35 pix/mm has been found to be sufficient for the f-stop number used in the experiments. The high sensitivity allows the use of small seeding particles that faithfully follow the flow. For our flow field of interest, a particle diameter of $0.5\,\mu$m and a frequency response of 200 kHz was found to be appropriate [14]. We use incense smoke, which mainly consists of oil droplets. A decantation system is used to suppress the residual solid particles generated during the combustion of the incense. Also, a field of view compatible with the extended flow field of the SWTBLI can be obtained (see Figure 11 in the results section). Two cameras, installed perpendicular to each other, view the same field of view due to a high-accuracy dual camera mount with a cubic prism. The cameras are installed on a micro-metric system each, allowing accurate adjustments in two degrees of freedom (horizontal and vertical displacement) for both cameras. The cubic prism can also be adjusted to allow an accurate alignment of the FoV for both cameras. Displacements of only $O(1\,\mathrm{pixel})$ over the full range can be obtained. This is small compared with the interrogation window size and especially with the whole field of view. Additionally, the rotation of the camera viewing the FoV indirectly can be adjusted accurately. Rotational errors were carefully assessed and found to be negligible (see next section).

With these high-resolution cameras and the comparatively powerful lasers, a much improved quality of the PIV data compared with previous systems is expected. This should allow accurate measurements of the wall normal turbulent fluctuation quantity, which is usually quite small and therefore extremely difficult to measure and resolve correctly [3]. A Fast Digital Converter is used for the synchronization of the two PIV systems, each consisting of a camera and a dual-head laser. The time delay between the two camera and laser systems can be arbitrarily chosen between $0 \leq \delta\tau < \infty$, with an error smaller than 10 ns, which is acceptable for high speed flows.

3 Validation of the technique and data quality

The accuracy of Dual-PIV measurement data depends on a number of things: 1) the ability of the particles to faithfully follow the flow, 2) the quality of the particle images, 3) the accuracy of the calculated particle displacements (i.e. the analysis algorithms), 4) the thickness and alignment of the laser sheets, 5) the general alignment of the two PIV systems, 6) the synchronization of the two PIV systems, and 7) the cross talk between the two cameras [13, 15]. Points 1 and 6 have been discussed in the previous section, the remaining points will be discussed in the following paragraphs. To validate the measurement technique, we carefully assessed the alignment of the two systems, the camera cross-pollution, as well as the inter-camera data consistency.

The system alignment was performed carefully, so that the same field of view (FoV) and spatial resolution were obtained in both systems, which is essential for the measurement technique. The overlap and alignment of the four laser sheets was assessed directly in the wind-tunnel test-section. A checker-board calibration target with a size of $168 \times 54\,\mathrm{mm}^2$ and a fluorescent surface was positioned in the selected measurement plane and location. The light sheets were then aligned such that the entire surface of the calibration target was uniformly illuminated. **In a second step, to ensure a precise alignment as well as to quantify the alignment, the light sheet was projected on a screen, recorded, and post-processed: a 2M Pixels PIV CCD camera was used for the recordings, then the amplitudes at different locations were compared for the four light sheets.** The location and thickness of the laser sheets was then carefully checked with a caliper gauge and a screen at multiple locations throughout an the extended field of view to verify that the thicknesses of all light sheets do not vary significantly over the entire field of view. The spacing between the laser light sheets was minimized as much as possible, typically displacements of less than a tenth of the light sheet thickness (1 mm) were obtained. The two cameras were then aligned on the calibration target by means of the orientation of the cubic prism and the micro-metric systems, such that the same fields of view and spatial resolutions were obtained. Care was also taken to check the parallelism of the laser sheets by verifying that both fields of view are exactly rectangular and the images were not distorted. The spatial resolution was constant over the field of view with an error $< 0.07\%$. The focus was then checked and adjusted on the particle images, also ensuring that the image quality is uniform throughout the entire field of view. These procedures were then repeated multiple times until the settings converged. A spatial resolution of 35 pixels/mm (96 pixels/displacement thickness) could be obtained with the current setup, which is satisfactory for the application in the Mach 2 SWTBLI flow field. The camera alignment and system alignment errors were assessed by means of the displacement field obtained for zero time delay $\delta\tau = 0\,\mu$s between the two systems. For this, the cross-correlation field between the first frame of camera 1 and the first frame of camera 2 – which should be exactly the same image – was calculated for 500 snapshots of seeding particles in the Mach 2 interaction and then averaged. The absolute mismatch between the fields of view of the cameras over the whole distance was a displacement in the streamwise x-direction of 2 pixels and a mean displacement of 0 pixels in the perpendicular y-direction (see Figure 4). This is small compared with the minimal interrogation window size of 32×16 pixels and especially the size of the FoV of 4008×1362 pixels. As mentioned previously, rotation was found to be negligible.

On the taken snapshots of the particle images, we also verified that the particle images span $3-4$ pixels on the CCD array, so that accurate sub-particle estimates of their locations can be obtained (see Adrian [16] and Raffel et al. [15]).

To quantify the laser-light cross-pollution between the four laser pulses and image frames, an image of the laser sheet on a screen has been taken with the respective laser tubes switched off for simultaneous measurements ($\delta\tau = 0\,\mu$s). The pixel intensity levels in the images were then compared with the background noise and are shown in the intensity histograms presented in Figure 5. The image of the laser sheet on a screen is much brighter than the images of the seeding particles, and the camera objectives had to be closed up to F22.0 in order to acquire pictures near the saturation of the CCD on 14 bits. This test thus corresponds to the worst-case scenario.

First, measurements were taken with both lasers switched off, in order to determine the noise of the respective camera's CCD. The resulting intensity histograms for cameras C1 and C2 are shown on the top left and right of Figure 5, respectively. Then the cross-talk, i.e. the cross-pollution of the laser corresponding to the second PIV system measured in the first and vice versa, was determined (see Figure 5 (c) and (d)). With a difference of about 30 to 40 points, it is only slightly above the CCD noise of the respective cameras. Finally, the actual measurement signal of the corresponding laser and camera systems, L1 in C1 and L2 in C2, was compared to the respective cross-pollution disturbance signal and CCD noise, as shown in the images in Figures 5 (e) and (f). Note that the intensity scales

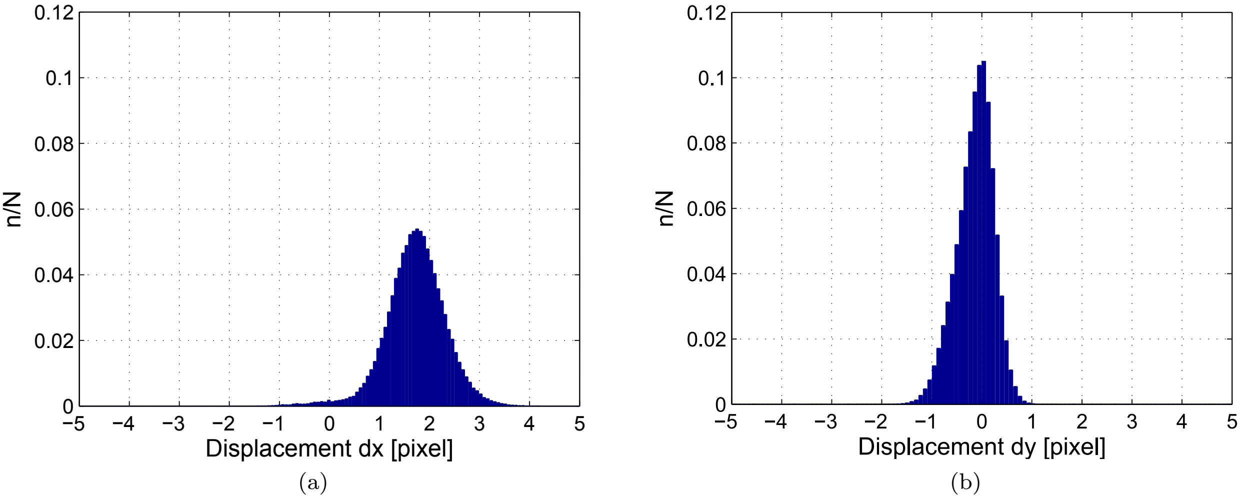

Fig. 4 Displacement histogram between the respective first frames of the two cameras for $\delta\tau = 0$ in the streamwise x-direction and wall normal y-direction.

are greatly increased compared with the top and center plots and therefore plotted in a semi-logarithmic representation for convenience. With intensity ratios between the cross-pollution and the measurement signal of 0.0075 and 0.004 for C1 and C2, respectively, the color filters' blockage is above 99% and the image separation can be considered as more than sufficiently effective. Similar tests have been performed with images of particles in the Mach 2 reflected shock interaction. For these experiments a F-stop of 4 was used. Some wall reflections of the laser sheets were present in the FoV, leading to locally high intensities but without blooming of the CCD. The particles' light was completely cut-off for both cameras when the attenuation of the wall reflections was of 96%.

To demonstrate the data accuracy obtained with the system, some results of a subsonic pre-study are shown. The system was developed and validated with a low-speed subsonic axisymmetric jet in a small calibration wind tunnel. The jet temperature was equal to the temperature of the surrounding fluid and the jet exited into quiescent air. Characteristics of the jet are summarized in table 1. This approach had several advantages: the experimental setup (as shown schematically in Figure 6) was easily accessible during the development phase, while allowing the qualification of the characteristics necessary for supersonic flows, and the flow field of the jet is well-known. Furthermore, the expected noise in the measurements of each individual PIV system is much lower for this type of axisymmetric, subsonic flow compared with the supersonic SWT-BLI flow field, where wall reflections and very large gradients are to expect, as well as lower seeding density.

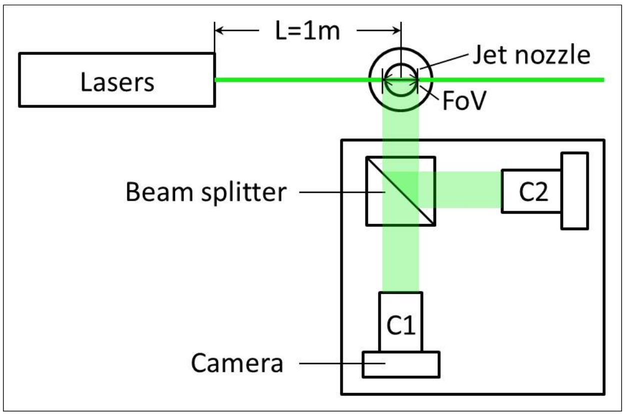

Fig. 6 Experimental setup of the Dual-PIV system at IUSTI during system development

Table 1 Characteristics of the subsonic jet. The given quantities are: Diameter of the circular orifice d, jet exit velocity U_j, Reynolds number Re_d based on the orifice diameter, and jet Mach number M_j (incompressible).

d	U_j	Re_d	M_j
30 mm	$5.0\,\frac{m}{s}$	9542	0.01

This allows the determination of the full potential of the measurement system. The axisymmetric jet has an initial mean jet velocity of $U_j = 5\,\frac{m}{s}$, coming from an orifice of $d = 30\,\text{mm}$ in diameter. The mean velocity is self-preserving beyond a distance of about $\frac{x}{d} = 8$ [17], which is well beyond the distance of $x = 3d$ observed for the present pre-study.

Of course, care was taken to develop the system with parameters that are usable in the supersonic flow fields for which the system is developed. The field of

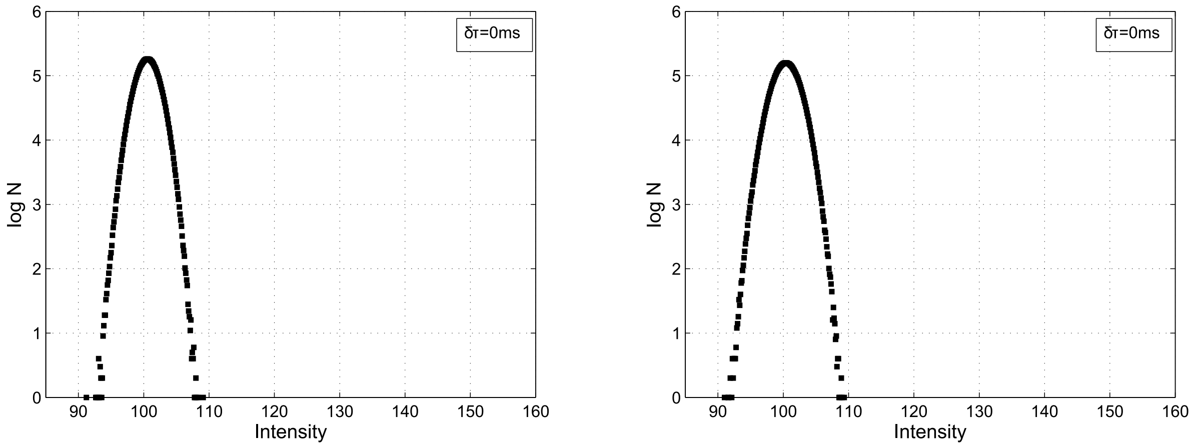

(a) CCD noise C1 (b) CCD noise C2

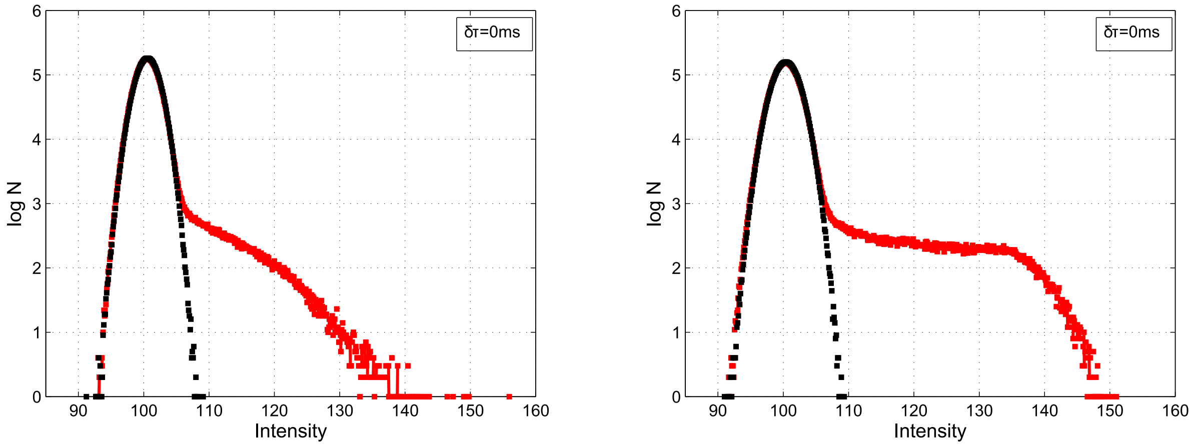

(c) Disturbance signal C1 (d) Disturbance signal C2

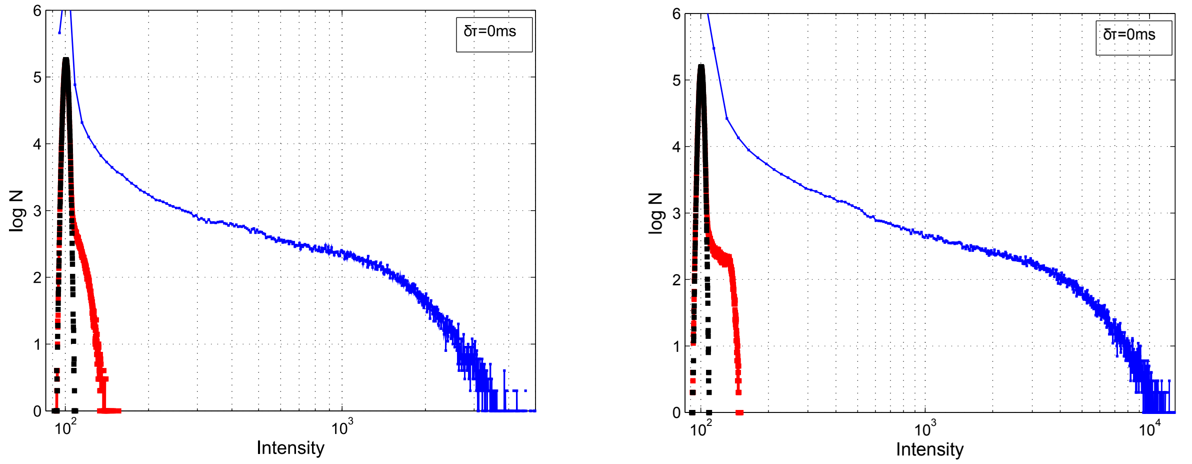

(e) Measurement signal C1 (f) Measurement signal C2

Fig. 5 Pixel intensity histograms for cameras C1 (left) and C2 (right). Top: CCD noise, both lasers switched off. Center left: Disturbance signal from laser L2 in camera C1 (red symbols) compared with the CCD noise (black). Center right: Disturbance signal from laser L1 in camera C2 (red symbols) compared with the CCD noise (black). Bottom left: Measured signal of laser L1 in camera C1 (blue symbols), compared with the disturbance signal from L2 (red) and the CCD noise (black); semi-logarithmic plot. Bottom right: Measured signal of laser L2 in camera C2 (blue symbols), compared with the disturbance signal from L1 (red) and the CCD noise (black); semi-logarithmic plot.

view, spatial resolution, and focal distance were thus set as required for the supersonic SWTBLI experiment. The flow was seeded with oil droplets from incense smoke with the same particle generator system also used for the high-speed experiments. This system provides a particle diameter of 0.5 μm and a frequency response of 200 kHz, which was shown to be appropriate for application in a Mach 2.3 SWTBLI very similar to our flow field of interest [14].

Conditional seeding with an injection of the particles into the calibration wind tunnel upstream of a honeycomb was chosen to be able to track turbulent eddies with the naked eye from raw PIV images. This does unfortunately give validation problems outside of the jet core, in regions that are not sufficiently seeded. However, since the aim of this subsonic jet pre-study is not the investigation of the flow physics of the jet itself, but the validation of the Dual–PIV measurement system, these shortcomings are not of primary concern.

Contour plots of the mean velocity U in the streamwise $x-$direction and the normal Reynolds stress component σ_u of this velocity component are shown in Figure 7. The characteristic laminar core of the jet is clearly recognizable, as well as the shear layer around it, where the turbulence level is strongly increased.

Inter-camera data consistency is shown with profiles of the standard deviation σ_u, shown in Figure 8 for a cut ($x = 1.33d$) through the investigated FoV for both cameras. The validation is given in valid vectors per total number of image pairs taken. In the regions of sufficient seeding density and thus validation, the profiles agree very well with each other ($-0.4 < \frac{y}{d} < 0.4$). This corresponds to a good agreement up to a turbulence intensity of 20%. Outside of the sufficiently seeded region, the two systems still show the same trends, but the quantitative agreement is not as good as in the region of high validation. All shown results were obtained from 1500 image pairs per camera. Three iterations with a minimal iteration window size of 16×16 pixels (at a spatial resolution of 35 pixels/mm) have been performed. Longitudinal evolutions along the jet axis ($y/d = 0$) of the mean and standard deviation of the longitudinal velocity are presented in Figure 8(b) for both PIV systems. A very good agreement between the systems can be observed for both quantities. As already shown in Figure 7(b), an increase of the velocity fluctuations can be observed from $x = 0.8D$ to $x = 2D$.

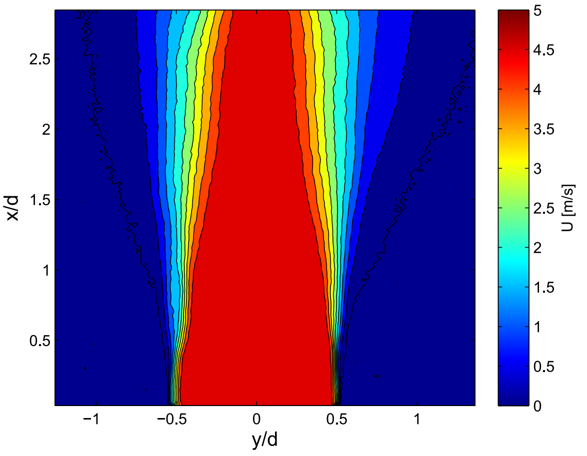

(a) U

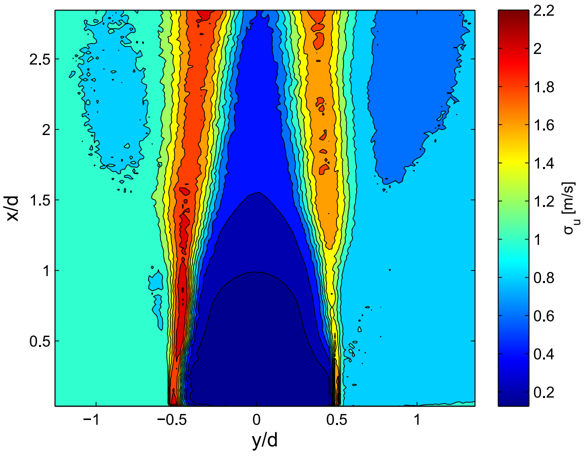

(b) σ_u

Fig. 7 Contour plots of the mean velocity U in the streamwise direction (top) and normal Reynolds stress component σ_u of the same quantity (bottom) for camera C1.

In order to assess the overall system noise and to determine the cycle duration, the auto-correlation coefficient $R(x,t)(x,t+\delta\tau)$ for a number of time delays $\delta\tau$ between the two PIV systems was calculated. The auto-correlation coefficient was calculated from the covariance between both cameras $\overline{u_1' u_2'}$ compared with the directly determined standard deviation values σ_{u_1} and σ_{u_2} for cameras 1 and 2, respectively,

$$R = \frac{\overline{u_1' u_2'}}{\sigma_{u_1}\sigma_{u_2}}$$

For $\delta\tau = 0\,\mu$s, these values depict the same quantity, and the deviation of R from unity is therefore a measure for the global system noise level, as well as the inter-camera data consistency. As expected, in the sufficiently seeded and validated zones of the flow (jet core), these quantities indeed have practically the same value for $\delta\tau = 0\,\mu$s, with an error of only -2%, and thus about 1% when standard deviations are considered (see zoom in Figure 9).

Figure 9 represents the auto-correlation coefficient for several locations around the center of the jet at $x = 1.33d$: $y = -0.2d$, $0.03d$, $0.1d$, and $0.23d$. The cor-

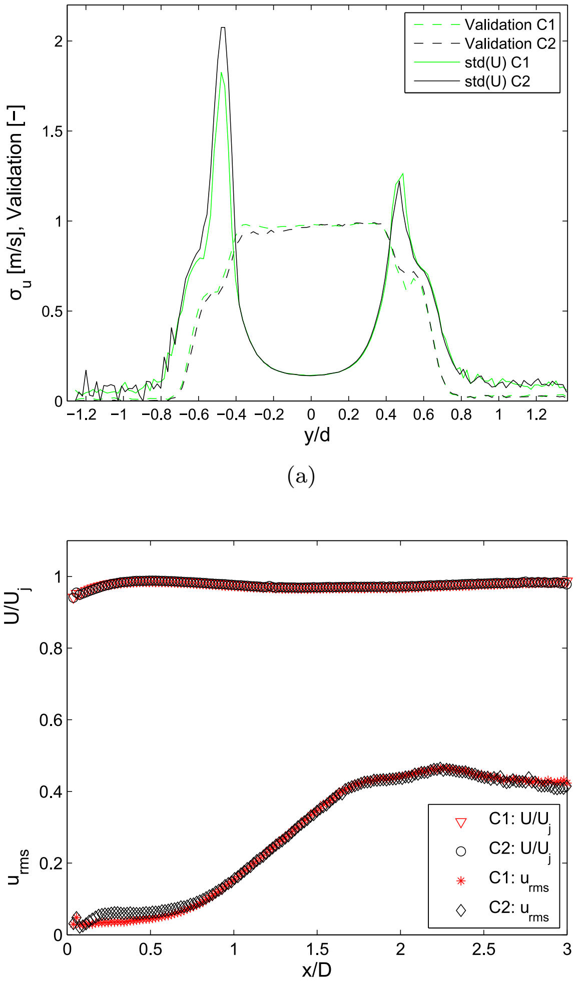

(a)

(b)

Fig. 8 a) Standard deviation and validation along a cut through the flow field for $x = 1.33d$ for both cameras, b) Mean streamwise velocity U/U_j (normalized with jet exit velocity) and rms of the fluctuating streamwise velocity component for both cameras.

relation coefficient is plotted for $\delta\tau = 0\,\mu$s and time delays ranging from $\delta\tau = 240\,\mu$s to 240 ms. The duration of one cycle is approximately 10 ms, corresponding to a characteristic frequency of 100 Hz for the larger scale turbulent eddies in the shear layer. This corresponds to a Strouhal number S_D of $S_D = fD/U_0 = 0.6$.

4 First results in a supersonic turbulent boundary layer

After validating the Dual-PIV system in the subsonic jet flow, first measurements were performed in the supersonic wind tunnel at the IUSTI laboratory at a Mach number of 2. This hypo-turbulent wind tunnel is a continuous facility with a closed-loop circuit. The facility has been used for detailed shock wave/boundary layer interactions studies, although with a different nozzle (see for example [2,14,18,19]). Present experiments are using a Mach 2 nozzle and a rectangular test section with a width of 170 mm and a height of 105 mm. A shock wave / boundary layer interaction flow field with a reflected shock wave is created, where the incident shock wave is generated by a sharp leading edge fixed on the ceiling of the test section. The present experiments were performed at a stagnation pressure of $P_0 = 0.4$ atm and a stagnation temperature of $T_0 = 290$ K. The experimental conditions are summarized in Table 2 and a Schlieren visualization of the flow field is presented in Figure 10.

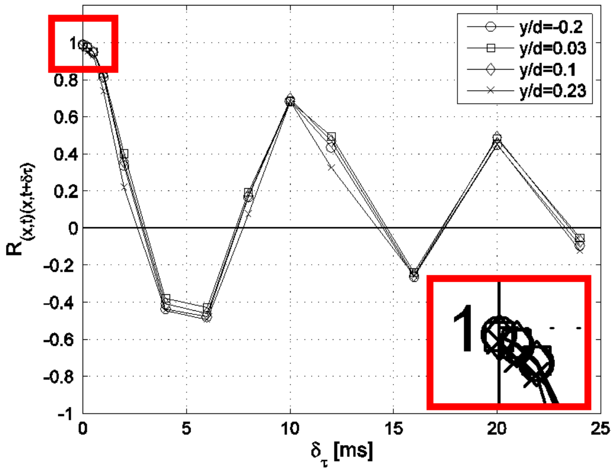

Fig. 9 Auto-correlation coefficient for several time delays $\delta\tau$ determined from the two systems for $x/d = 1.33$ and different spanwise locations $(-0.2d \leq y \leq 0.23d)$ with in the well-validated zone of the flow field.

Table 2 Experimental conditions for the Mach 2 interaction flow field. The given quantities are: Mach number M, free-stream velocity U_e at the boundary layer edge, momentum-thickness based Reynolds number Re_θ, stagnation pressure p_0, stagnation temperature T_0, and deflection angle θ.

M	U_e	Re_θ	P_0	T_0	θ
1.98	505 $\frac{m}{s}$	4462	0.4 atm	290 K	8.75°

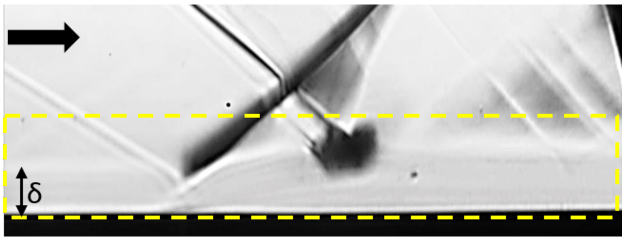

Fig. 10 Schlieren optic visualization of the reflected shock interaction at Mach 2. Flow direction is from left to right. The field of view for the PIV measurements is marked in yellow.

In order to minimize flow perturbations, the boundary layer is seeded with incense smoke droplets through openings in the wind tunnel floor upstream of the nozzle. The flow outside of the boundary layer is thus not seeded.

The boundary layer results presented here, were derived from a validation database of 500 image pairs for each time delay $\delta\tau = 0$. Smooth curves are thus not to expect. However, the data are suitable to demonstrate the applicability of the developed Dual-PIV system for measurements in supersonic shock wave / turbulent boundary layer interactions. The minimal interrogation window size was 32×16 pixels ($= 0.9\times0.45$ mm $= 0.09\delta \times 0.05\delta$) with 50% overlap.

One requirement on the system was the capability to provide a field of view sufficiently large to show the interaction region and either the incoming boundary layer or the boundary layer downstream of the interaction, while also providing satisfactory spatial resolution.

This was achieved: Figure 11 shows contour plots of the mean streamwise velocity component U and normal Reynolds stress component σ_v for the investigated interaction case with the largest separated region (deflection angle $\theta = 8.75°$). The incoming boundary layer (flow direction is from left to right) and separated region are clearly recognizable and a sufficiently seeded field of view of 110×18 mm was obtained (see yellow marks in Figure 10). The boundary layer is seeded at the wall upstream of the sonic nozzle to minimize boundary layer perturbation. Therefore, the external flow is not seeded. Long experience with LDA measurements showed that this method of seeding minimizes wall-shear stress perturbations in the turbulent boundary layer. Zones with unsatisfactory validation (less than 45% of valid vectors) towards the free-stream appear in white in Figure 11. In general, the percentage of valid vectors across the flow field is between 80-98%. Lower validation is only a problem towards the boundary layer edge, since the free-stream was not seeded. (The white zone near the wall in Figure 11 (a) represents negative streamwise mean velocity.)

The second requirement that the system absolutely had to fulfill, was sufficient data quality and spatial resolution to accurately measure turbulent quantities in supersonic flows. This was assessed with the incoming supersonic boundary layer upstream of the interaction. The boundary layer characteristics, as determined from the current measurements, are presented in Table 3.

Table 3 Characteristics of the incoming turbulent boundary layer at Mach 2. The given quantities are: Boundary layer thickness δ_{99}, displacement thickness δ^*, momentum thickness θ, friction velocity u_τ (determined with the Clauser chart method [20]), friction coefficient c_f, and shape factor H.

δ_{99}	δ^*	θ	u_τ	c_f	H
10.5 mm	2.75 mm	0.85 mm	21.9 $\frac{m}{s}$	0.0023	3.24

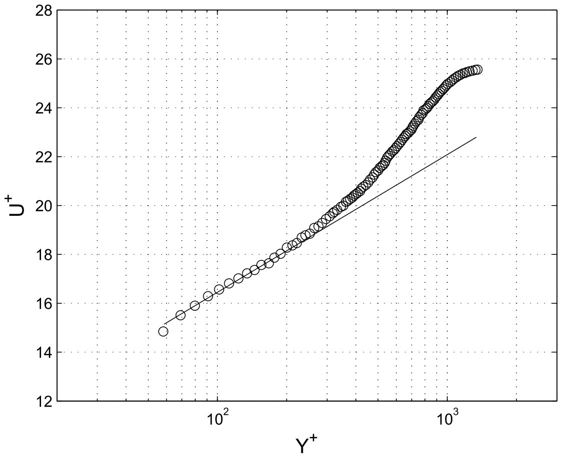

Fig. 12 Profile of the mean velocity U in the streamwise direction across the Mach 2 boundary layer, transformed according to van Driest (symbols) and compared with the log-law (solid line).

The mean velocity profile transformed according to van Driest is shown in Figure 12, and the turbulent intensity and Reynolds shear stress profiles across the boundary layer are shown in Figures 13 and 14, respectively. The van Driest transformed profile shows the expected good agreement with the log-law

$$U^+ = \frac{1}{k}\log(Y^+) + C, \tag{1}$$

with $k = 0.41$ and $C = 5.25$ between $40 \leq Y^+ \leq 200$ (see [3]).

The turbulent intensities in Morkovin scaling are compared to incompressible boundary layer measurements in Figure 13. Morkovin scaling takes density variation in compressible flow into account and is defined as follows:

$$\sqrt{\frac{\rho}{\rho_w}} \cdot \frac{\sqrt{\overline{u'^2}}}{u_\tau}, \sqrt{\frac{\rho}{\rho_w}} \cdot \frac{\sqrt{\overline{v'^2}}}{u_\tau}, \sqrt{\frac{\rho}{\rho_w}} \cdot \frac{\overline{(u'v')}}{u_\tau^2}. \tag{2}$$

The intensity profiles show the expected trends. The value of the u' component is slightly higher than the incompressible value.

For the wall-normal fluctuation component, the magnitude remains slightly below the subsonic value, while the profile shape is as expected for a turbulent boundary layer. Similar conclusions can be draw for the Reynolds shear stresses shown in Figure 14.

These results clearly show that the measurement system is able to provide PIV data of high quality and

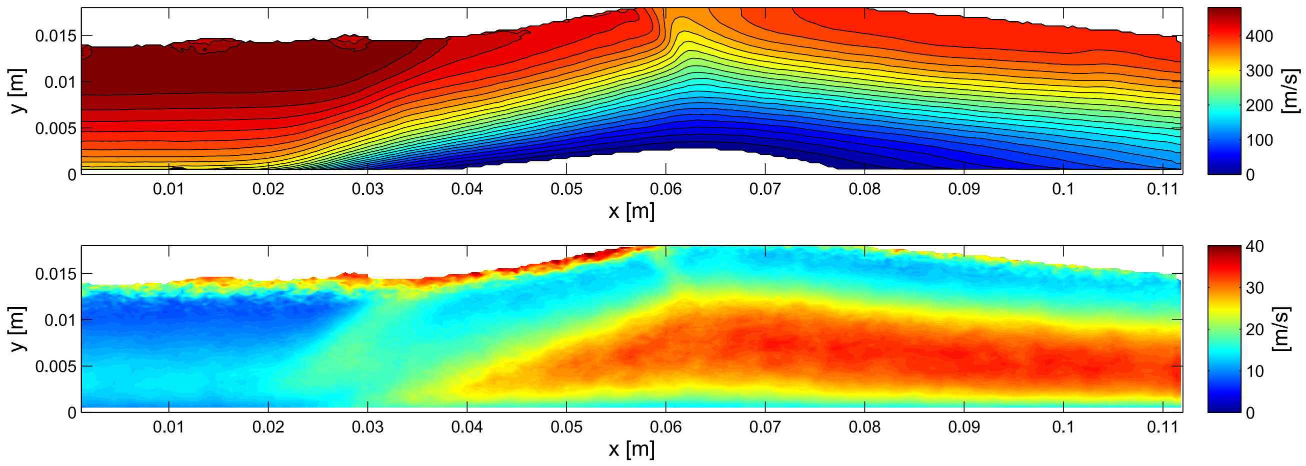

Fig. 11 Contour plot of the mean velocity U in the streamwise direction x across the interaction at Mach 2 (top) and of the root-mean-square value σ_v of the wall-normal velocity component v. Flow direction is from left to right. Negative mean velocity (recirculation zone near the wall) is marked in white in the U contour plot. In the free-stream, zones with unsatisfactory validation are also marked in white.

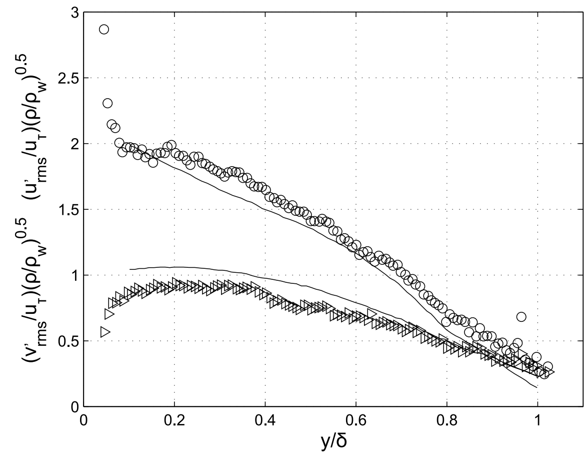

Fig. 13 Turbulence intensity profiles of the streamwise and wall-normal velocity components u' and v', respectively, in Morkovin scaling (symbols), compared with subsonic data from Klebanoff [21] (solid line).

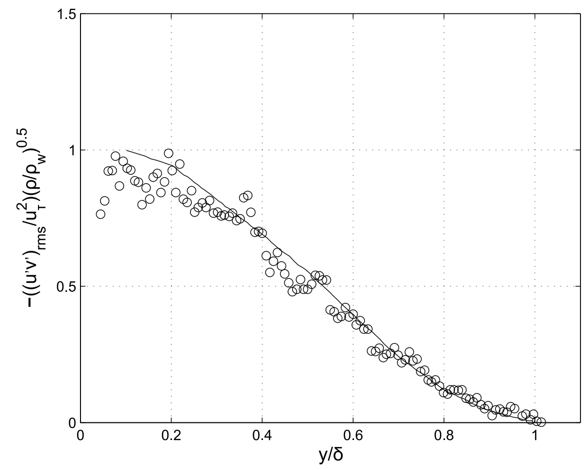

Fig. 14 Turbulent shear stress profiles in the incoming boundary layer in Morkovin scaling (symbols), compared with subsonic data from Klebanoff [21] (solid line).

can be successfully applied for measurements in supersonic turbulence.

The third and fourth major system requirements referred to the temporal delay between the systems – which has to be sufficiently small to obtain temporal information in a high-speed flow – and the overall system-noise level, respectively. The latter was already assessed based on the image separation quality (see Figure 5) and the jet flow study (see Figure 9), and the quality and potential of the developed system was clearly demonstrated. The next step was thus to assess this in the much more complex flow field of a supersonic shock wave/turbulent boundary layer interaction. To do so, the auto-correlation function of the PIV signal in the reattachment zone of the interaction (corresponding to location $x = 0.075\,\mathrm{m}$ in Figure 11) was reconstructed from measurements with the two PIV systems.

The results for 10 and 25 temporal delays between $0 \leq \delta\tau \leq 3500\,\mu\mathrm{s}$ are shown in Figures 15 (a) and (b), respectively.

The deviation from unity for $\delta\tau = 0$ is a measure of the noise, and system-noise values between 2% and 6% (1% and 3% for RMS) are obtained, which is quite good (see Figure 15 (a)).

In the reattachment zone (see Figure 15), the integral time scale is about $T = 250\,\mu\mathrm{s}$, which corresponds to a characteristic frequency of $\cong 4\,\mathrm{kHz}$ and

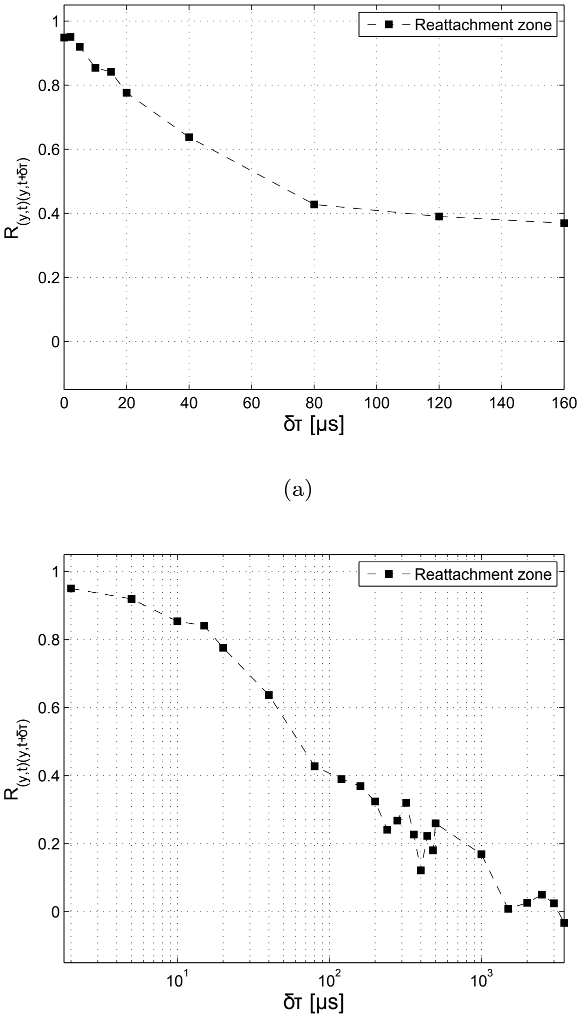

(a)

(b)

Fig. 15 Measured auto-correlation coefficient for a location in the reattachment zone of the separation bubble.

a Strouhal number, based on the interaction length and the external velocity downstream of the incident shock, of $St \cong 0.5$. This can be explained with the development of coherent structures in this vortex shedding zone, which is in good agreement with literature (Dupont et al. [2], Souverein et al. [8]). More important from a system development point of view is, that we are indeed able to obtain sufficiently small temporal delays (i.e. smaller than the integral scale) between the PIV systems. This is also true for a turbulent Mach 2.0 flat plate boundary layer, where an integral time scale of $T = O(10\,\mu\mathrm{s})$ is expected [3]. Overall, this is very encouraging and shows that the system gives access to spatio-temporal information in complex supersonic flows.

5 Conclusions

The development and validation of a new Dual-PIV system for accurate turbulence measurements in turbulent high-speed flows was shown and discussed. The system is intended to be applied for measurements in a Mach 2 shock wave/turbulent boundary layer interaction flow field, from which we intend to determine the space-time links between the flow phenomena in the separation bubble and the low-frequency shock motion. The setup of the experimental system was described, and we showed that a high accuracy in the system alignment as well as the image separation can be obtained with the current setup. The low measurement-noise level was demonstrated on the basis of directly measured and rebuild rms-values. We presented and discussed several time-frequency quantities derived from measurements in a low-speed subsonic jet flow field applied for the validation of the system, as well as preliminary results for a Mach 2 turbulent boundary layer, both clearly showing the potential of the developed system.

Acknowledgements This work received financial support by the CNES within the research program ATAC, the ANR within the program DECOMOS, and also the Labex MEC. This support is gratefully acknowledged.

References

1. D. S. Dolling, Fifty years of shock-wave/boundary layer interaction research: what next?, AIAA Journal, 39 (8), pp. 1517–1531 (2001).
2. P. Dupont, C. Haddad, and J.-F. Debiève, Space and time organization in a shock-induced separated boundary layer, Journal of Fluid Mechanics (559), pp.255–277 (2006).
3. A. J. Smits, J.-P. Dussauge, Turbulent Shear Layers in Supersonic Flow, Second Edition. Springer Science+Business Media Inc, New York, NY (2006).
4. V. Fleury, C. Bailly, E. Jondeau, M. Michard, D. Juve, Space-Time Correlations in Two Subsonic Jets Using Dual Particle Image Velocimetry Measurements, AIAA Journal, 46 (10), pp. 2498-2509 (2008).
5. J. Bridges, M. Wernet, Measurements of Aeroacoustic Sound Sources in Turbulent Jets, In: AIAA/CEAS Aeroacoustics Conference and Exhibit, Hilton Head, South Carolina, 12-14 May 2003.
6. J. Bridges, Effect of Heat on Space-Time Correlations in Jets, In: 12th AIAA/CEAS Aeroacoustics Conference, Cambridge, Massachusetts, 8-10 May 2006.
7. P. Guibert, L. Lemoyne, Dual particle image velocimetry for transient flow field measurements, Exp Fluids, 33 (2), pp. 355–367 (2002).
8. L. J. Souverein, B. W. van Oudheusden, F. Scarano, P. Dupont, Application of a dual-plane particle image velocimetry (dual-PIV) technique for the unsteadiness characterization of a shock wave turbulent boundary layer interaction, Measurement Science and Technology, 20, pp. 1–16 (2009).

9. B. Ganapathisubramani, E. K. Longmire, I. Marusic, S. Pothos, Dual-plane PIV technique to determine the complete velocity gradient tensor in a turbulent boundary layer, Experiments in Fluids, 39 (2), pp. 222-231 (2005).
10. H. Hu, T. Saga, T. Kobayashi, N. Taniguchi, M. Yasuki, Dualplane stereoscopic particle image velocimetry: system set-up and its application on a lobed jet mixing flow, Exp Fluids, 31, pp.277–293 (2001).
11. C. J. Kähler, J. Kompenhans, Fundamentals of multiple plane stereo particle image velocimetry, Experiments in Fluids, 29 (1 Supplement), pp. S070–S077 (2000).
12. C. J. Kähler, Investigation of the spatio-temporal flow structure in the buffer region of a turbulent boundary layer by means of multiple plane stereo PIV, Experiments in Fluids, 36, pp.114–130 (2004).
13. J. A. Mullin, W. J. A. Dahm, Dual-plane stereo particle image velocimetry (DSPIV) for measuring velocity gradient fields at intermediate and small scales of turbulent flows, Experiments in Fluids, 38 (2), pp. 185–196 (2005).
14. S. Piponniau, J.-P. Dussauge, J.-F. Debiève, P. Dupont, A simple model for low-frequency unsteadiness in shock-induced separation, Journal of Fluid Mechanics, 629, pp. 87–108 (2009).
15. M. Raffel, C. Willert, S. Wereley, J. Kompenhans, Particle Image Velocimetry - A practical guide, Second Edition. Springer, (2007).
16. R. J. Adrian, Dynamic ranges of velocity and spatial resolution of particle image velocimetry, Measurement Science and Technology 8(12), pp. 1393–1398 (1997).
17. H. Tennekes, J. L. Lumley, A first course in turbulence. The MIT Press, Cambridge, Massachusetts (1972).
18. J.-F. Debiève, P. Dupont, Dependence between the shock and the separation bubble in a shock wave boundary layer interaction, Shock Waves, 19, pp.499–506 (2009).
19. P. Dupont, C. Haddad, J. P. Ardissone, J.-F. Debiève, Space and time organization of a shock wave/turbulent boundary layer interaction, Aerospace Science and Technology, 9(7), pp.561–572 (2005).
20. F. H. Clauser, Turbulent Boundary Layers in Adverse Pressure Gradients, Journal of the Aeronautical Sciences, 21(2), pp. 91–108 (1954).
21. P. S. Klebanoff, Characteristics of turbulence in a boundary layer with zero pressure gradient, NACA Report 1247 (1955).